# Output Feedback $H_{\infty}/GH_2$ Control For In-Wheel Motor Driven Semi-Active Suspensions With Nonlinear Constraints

Journal Title
XX(X):1–10
©The Author(s) 2025
Reprints and permission:
sagepub.co.uk/journalsPermissions.nav
DOI: 10.1177/ToBeAssigned
www.sagepub.com/

SAGE

Jie Guo<sup>2</sup>, Chao Ma<sup>2</sup>, Shuyou Yu<sup>1,2</sup>, Ye Zhuang<sup>1</sup> and Hong Chen<sup>3</sup>

#### **Abstract**

The increased unsprung mass in In-Wheel Motor (IWM) driven semi-active suspension systems leads to degraded handling stability and ride comfort. In this paper, an output feedback  $H_{\infty}$ / generalized  $H_2$  ( $GH_2$ ) control strategy is proposed for semi-active suspensions equipped with Magneto-Rheological (MR) dampers to attenuate vertical vibration. The  $H_{\infty}$  norm is used to evaluate the closed-loop performance, while the  $GH_2$  norm is applied to limit hard constraints of the system. A major challenge arises from the dissipative characteristic of the MR damper, which introduces nonlinear constraints that complicate optimal control design and limit performance improvements. To address this issue, the allowable damping force range of the MR damper is identified through MTS850 testbed experiments. Subsequently, a piecewise controller is designed to approximate the nonlinear constraint as piecewise constant bounds. The effectiveness of the proposed control strategy has been validated by simulation results.

#### **Keywords**

In-wheel motor driven electric vehicles, semi-active suspension,  $H_{\infty}/GH_2$  control, nonlinear constraint.

#### Introduction

Energy consumption, environmental pollution, and climate change have become increasingly critical issues in recent years. New energy vehicles (NEVs) are seen as an important solution to these challenges. The transition from internal combustion engine vehicles to electricity driven motors stands out as a significant development (Mishra et al., 2022).

Based on the propulsion system, electric vehicles can be roughly classified into centralized motor driven electric vehicles and IWM driven electric vehicles (Cai et al., 2022). The internal combustion engine is replaced with a drive motor for the centralized motor-driven electric vehicles, which is then integrated with a traditional transmission system. While the technology has been well-established, it suffers from low transmission efficiency and larger size (Xiao et al., 2024). In contrast, a distributed drive system is employed in IWM driven electric vehicles, where the motor is directly integrated into the wheel. It eliminates the need for complex gearboxes, transmission, and differential mechanisms, and simplifies the mechanical structure of the chassis, attracting significant attention from researchers (Huynh et al., 2022).

However, since the motor is directly integrated into the wheel, the increased unsprung mass causes changes of the system's dynamic characteristics, leading to degraded road holding and ride comfort performance (Mahmouditabar et al., 2022). To address this issue, (Nagaya et al., 2003) innovatively proposes the dynamic-damping IWM driven system, which suspends the shaftless direct-drive motor and isolates it from the unsprung mass. (Li et al., 2019; Qin et al., 2018) conduct dynamic analysis for IWM driven electric vehicles with this type of structure. The results indicate that, compared to traditional configurations, the dynamic-damping IWM driven system effectively attenuates

the negative vibration caused by the increased unsprung mass. Otherwise, road holding and ride comfort remain in conflict with each other. Active and semi-active suspensions have been recognized as promising approaches to provide a trade-off between these conflicts. Several active control techniques, such as fuzzy  $H_{\infty}$  control (Shao et al., 2017), finite-frequency  $H_{\infty}$  control (Jin et al., 2023), and preview nonlinear model predictive control (Vidal et al., 2022), have been proposed to improve the performance of IWM driven electric vehicles. Due to the high cost and significant energy consumption associated with active suspension systems, they are currently limited to a small number of high-end vehicles (Zhang and Su, 2024). In contrast, semi-active suspension systems, which regulate suspension dynamics through controllable dampers, have notable advantages, including low energy consumption and superior control performance (Min and Wei, 2024). Therefore, semi-active suspension systems have attracted significant attention (Yuan et al., 2023), particularly Magneto-Rheological (MR) semiactive suspensions (Jin et al., 2020; Ma et al., 2024).

For MR semi-active suspension systems, the dissipative characteristic of the damper, which introduces a nonlinear constraint, presents a critical challenge that should be

#### Corresponding author:

Shuyou Yu, Jilin University, No.5988, Renmin Road, Nanguan District, Changchun 130012, Jilin, China.

Email: shuyou@jlu.edu.cn

<sup>&</sup>lt;sup>1</sup>State Key Laboratory of Automotive Simulation and Control, Jilin University, Changchun, China

 $<sup>^2</sup>$ Department of Control Science and Engineering, Jilin University, Changchun, China

<sup>&</sup>lt;sup>3</sup>College of Electronics and Information Engineering, Tongji University, Shanghai, China

addressed during the controller design and optimization process. "Clipped-optimal control" is widely used, where the optimal control force is first computed but then modified by a clipping strategy based on actuator constraints (Yang et al., 2023; Savaia et al., 2021; Ma et al., 2019; Yoon et al., 2021; Ding et al., 2023). However, this alteration deviates from optimal control principles, limiting further performance improvements. Subsequently, a piecewise affine  $H_{\infty}$  controller is proposed in (Wu et al., 2019). However, all conflicting requirements are integrated into a single weighted cost function. The selection of appropriate weighting matrices can be challenging. Fractional-order sliding mode control methods proposed by (Nguyen et al., 2020) and (Nguyen et al., 2021) have demonstrated enhanced robustness and flexibility. Nonetheless, directly accommodating input and state constraints remains challenging. (Wu et al., 2020) designs a hybrid horizon varying MPC strategy for vehicle speed planning in semi-active suspension systems. A dynamic programming-based solution is provided, but it still requires considerable computational resources. (Lee et al., 2023) proposes a model-free deep reinforcement learning control algorithm for semi-active suspension, where the controller is trained directly from experimental data. The performance is limited by the quality and quantity of the data.

In summary, MR semi-active suspensions can effectively attenuate the deterioration of ride comfort and handling stability caused by the increased unsprung mass in IWM driven electric vehicles. The nonlinear constraint of the MR damper remain challenging. Moreover, the tradeoff between suspension system performance and actuator limitations requires further optimization. To address this issue, this paper proposes an output feedback  $H_{\infty}/GH_2$ control strategy. The  $H_{\infty}$  norm is used to minimize the vertical acceleration of the sprung mass to improve ride comfort, while the  $GH_2$  norm is utilized to limit hard constraints of the system. Specifically, an output feedback solution to the control problem is formulated within the context of linear matrix inequality (LMI) optimization and multi-objective control. In addition, the nonlinear constraint is described using a piecewise linearization method, followed by modeling the system as a linear affine system. Scope information is introduced to reduce the conservatism. Simulation results demonstrate that the piecewise linearization method effectively addresses the dissipative constraints of the MR semi-active suspension. The proposed controller achieves an optimal trade-off between ride comfort, handling stability, and the constraints on suspension stroke and the performance limits of the MR damper.

#### **Problem statement**

The quarter-vehicle IWM driven semi-active suspension system model, as shown in Fig.1, can be represented as:

$$\begin{split} m_{s}\ddot{x}_{s} + k_{s}\left(x_{s} - x_{u}\right) + c_{s}\left(\dot{x}_{s} - \dot{x}_{u}\right) &= u(t) \\ m_{u}\ddot{x}_{u} + k_{t}\left(x_{u} - x_{r}\right) - k_{s}\left(x_{s} - x_{u}\right) - c_{s}\left(\dot{x}_{s} - \dot{x}_{u}\right) \\ - k_{d}\left(x_{d} - x_{u}\right) - c_{d}\left(\dot{x}_{d} - \dot{x}_{u}\right) &= -u(t) \\ m_{d}\ddot{x}_{d} + k_{d}\left(x_{d} - x_{u}\right) + c_{d}\left(\dot{x}_{d} - \dot{x}_{u}\right) &= 0 \end{split} \tag{1}$$

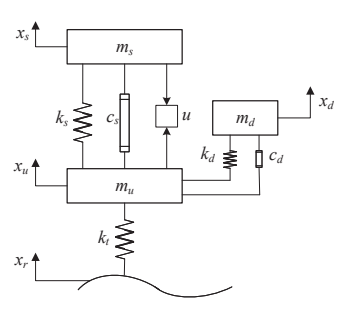


Figure 1. IWM driven semi-active suspension model.

The numerical values of the suspension parameters are given in Table 1.  $x_s, x_u, x_d$ , and  $x_r$  represent the vertical displacements of the vehicle body, wheel, motor, and road respectively. u(t) is the MR damping force.  $\dot{x}_{def} = \dot{x}_s - \dot{x}_u$  represents the deflection velocity, which also corresponds to the piston velocity of the damper.

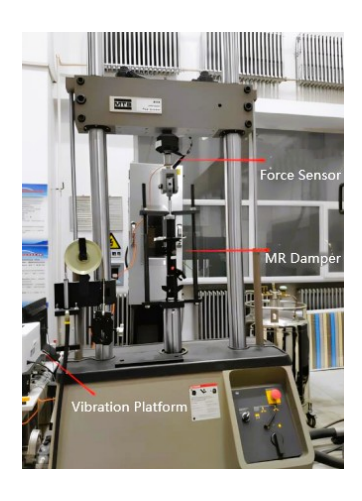


Figure 2. MTS850 testbed.

The characteristics of the MR damper are measured on the MTS850 testbed, as shown in Fig.2, following the automotive shock absorber testing method QC/T 545-1999.

The displacement sensor used is a BRT38-4M/5M, manufactured by ShenZhen Briter Technology Co.Ltd. The velocity is obtained by differentiating the displacement signals. The acceleration is measured with two ADXL202 modules from Analog Devices. All sensors are calibrated and filtered to ensure measurement accuracy.

In the external characteristic test, the input signals include piston stroke, piston velocity, and control current. The damper used is RD-8041-1. The piston stroke is selected as a sinusoidal signal with an amplitude of 0.08m, and the maximum excitation velocity is set to 1.6m/s. The applied control current ranges from 0 to 1A, with increments of 0.1A. The piston velocity/damping force characteristics is shown in Fig. 3. It can be seen that:

 (i) The damping force of the MR damper exhibits significant hysteresis characteristics in relation to the piston velocity and the current. Moreover, the hysteresis becomes more pronounced as the current value increases;

(ii) The damping force is approximately available in the first and third quadrants of the piston velocity/damping force coordinate system, i.e., dissipative constraint;

(iii) The damping force is asymmetric with respect to the origin.

Therefore, the design of the suspension controller should optimize suspension performance while ensuring that the damping force generated by the control law adheres to the limitations of the MR damper, including its saturation and dissipative characteristics.

**Remark 1:** To describe the hysteresis characteristics of the MR damper, the control current is selected from 0 to 1A with increments of 0.1A. However, the actual current is continuous. Therefore, the feasible damping force region is approximately represented by the shaded area in Fig.3. It is derived from experimental data and constrained by the testbed. This region is closely related to the piston's maximum velocity, maximum stroke, and current range. If these parameters remain unchanged, the feasible damping force region also remains fixed.

Notably, it's difficult to design a controller for system (1) with nonlinear constraints. If "clipped" control is applied, the problem becomes unconstrained, which renders the optimal control meaningless.

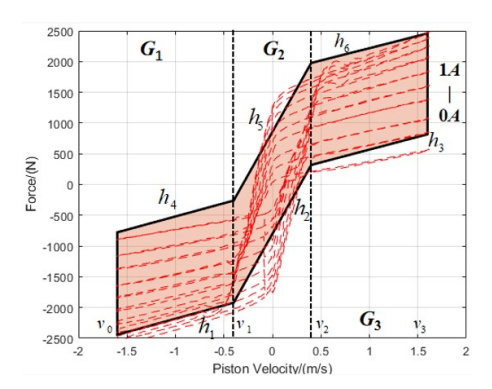


**Figure 3.** Piston Velocity/damping force characteristic of the MR damper.

To address nonlinear constraints in optimal control, a piecewise linearization method is used to provide a quantitative description of the available scope of u(t). According to Fig.3, the piston velocity is divided into three regions, i.e.,  $[v_0, v_1]$ ,  $(v_1, v_2)$ ,  $[v_2, v_3]$ . The envelopes of the available scope are approximated by the following six lines:

$$h_i(\dot{x}_{def}) = a_i + b_i \dot{x}_{def}, i = 1, \dots, 6$$
 (2)

where  $a_i$  and  $b_i$  are constants, and the values are shown in Table 2. For  $v_0 \le \dot{x}_{def} \le v_3$ , u(t) can be expressed by

$$\begin{array}{ll} h_{1}\left(\dot{x}_{def}\right) \leq u \leq h_{4}\left(\dot{x}_{def}\right) & v_{0} \leq \dot{x}_{def} \leq v_{1} \\ h_{2}\left(\dot{x}_{def}\right) \leq u \leq h_{5}\left(\dot{x}_{def}\right) & v_{1} < \dot{x}_{def} < v_{2} \\ h_{3}\left(\dot{x}_{def}\right) \leq u \leq h_{6}\left(\dot{x}_{def}\right) & v_{2} \leq \dot{x}_{def} \leq v_{3} \end{array} \tag{3}$$

Therefore, the dynamic model of the IWM driven semiactive suspension system (1) with the nonlinear constraint can be transformed into a piecewise linear system with piecewise constant constraints.

Table 1. Parameter numerical values of the suspension.

Description	Symbol	Value
Sprung mass	$m_s$	320kg
Unsprung mass	$m_u$	40kg
Motor mass	$m_d$	10kg
Stiffness	$k_s$	18000 N/m
Damping	$c_s$	1000Ns/m
Tire stiffness	$k_t$	200000N/m
Stiffness	$k_d$	50000N/m
Damping	$c_d$	2000Ns/m

**Table 2.** Parameter numerical values of  $a_i$ ,  $b_i$ 

i	1	2	3	4	5	6
	$-1747 \\ 433$					

# Control objectives

The control objectives of the suspension system are summarized as follows:

- (i) Ride comfort: minimize the vertical acceleration of the sprung mass  $\ddot{x}_s$  to enhance ride comfort.
- (ii) Handling stability: the dynamic tire load should not violate the static load in order to maintain handling stability.

$$k_t(x_u - x_r) < (m_s + m_u + m_d)g$$

(iii) Suspension stroke: because of the mechanical structure, the suspension stroke should not violate the allowable maximum value.

$$|x_s - x_u| < S_{max}$$

(iv) Actuator limitations: the constraints shown in Fig.3 should be satisfied.

# Output feedback $H_{\infty}/GH_2$ Control

# Piecewise linear system with linear constraints

According to the nonlinearity characteristics of the MR damper shown in Fig.3, the available scope is first divided into three regions:  $G_1, G_2$ , and  $G_3$ . Each region is further equally partitioned into  $N_a, N_b, N_c$  segments, respectively. The segmentation ensures that within each small interval, the system's nonlinear constraints can be approximated by linear constant constraints, thereby enabling the proposed  $H_{\infty}/GH_2$  control strategy. Additionally, the scope containing the origin is taken as symmetric with respect to the origin. The total number of partition is then given by:

$$N = N_a + N_b + N_c \tag{4}$$

Define  $j \in \{1, 2, ..., N\}$  as the index of the system partitions. The left boundary of  $\dot{x}_{def}$  for the j-th partition is given by:

$$x_{Lj} = \begin{cases} v_0 + \frac{(v_1 - v_0)(j - 1)}{N_a}, & j \le N_a \\ v_1 + \frac{(v_2 - v_1)(j - N_a - 1)}{N_b}, & N_a < j \le N_a + N_b \\ v_2 + \frac{(v_3 - v_2)(j - N_a - N_b - 1)}{N_c}, & N_a + N_b < j \le N \end{cases}$$
(5)

The right boundary of  $\dot{x}_{def}$  for the j-th partition is:

$$x_{Rj} = \begin{cases} v_0 + \frac{(v_1 - v_0)j}{N_a}, & j \le N_a \\ v_1 + \frac{(v_2 - v_1)(j - N_a)}{N_b}, & N_a < j \le N_a + N_b \\ v_2 + \frac{(v_3 - v_2)(j - N_a - N_b)}{N_c}, & N_a + N_b < j \le N \end{cases}$$

The upper and lower bounds of the damping force for the j-th partition are:

$$\overline{F_j} = h_{m_1}(x_{Lj}), \quad m_1 = 4, 5, 6$$
  
 $F_j = h_{m_2}(x_{Rj}), \quad m_2 = 1, 2, 3$ 

Based on the above analysis, piecewise constant constraints are introduced to integrate system constraints into the controller design.

According to system (1), the state vector is defined as  $x = \begin{bmatrix} x_s - x_u & \dot{x}_s & x_u - x_r & \dot{x}_u & x_d - x_u & \dot{x}_d \end{bmatrix}^T$ . The state-space equation for each partition is established:

$$\dot{x}(t) = \bar{A}x(t) + \bar{B}_1w(t) + \bar{B}_2u_j(t)$$

$$x(t) \in \aleph_i, u_i(t) \in \mathfrak{J}_i$$
(7)

where  $\aleph_j := \{x \mid x_{Lj} \leq x_2 - x_4 \leq x_{Rj}\}$ , is the domain of the j-th partition. The constant constrain is defined as  $\mathfrak{J}_j := \left\{u_j \mid \underline{F_j} \leq u_j \leq \overline{F_j}\right\}$ . The system matrices are as follows:

$$\bar{A} = \begin{bmatrix} 0 & 1 & 0 & -1 & 0 & 0\\ \frac{-k_s}{m_s} & \frac{-c_s}{m_s} & 0 & \frac{c_s}{m_s} & 0 & 0\\ 0 & 0 & 0 & 1 & 0 & 0\\ \frac{k_s}{m_u} & \frac{c_s}{m_u} & \frac{-k_t}{m_u} & \frac{-(c_s+c_d)}{m_u} & \frac{k_d}{m_u} & \frac{c_d}{m_u}\\ 0 & 0 & 0 & -1 & 0 & 1\\ 0 & 0 & 0 & \frac{c_d}{m_d} & \frac{-k_d}{m_d} & \frac{-c_d}{m_d} \end{bmatrix},$$

$$\bar{B}_1 = \begin{bmatrix} 0 & 0 & -1 & 0 & 0 & 0 \end{bmatrix}^T,$$

$$\bar{B}_2 = \begin{bmatrix} 0 & 1/m_s & 0 & -1/m_u & 0 & 0 \end{bmatrix}^T$$

Consistent with the control objectives, the outputs of the suspension system are defined as:

## (i) Control output:

$$y_1(t) = \ddot{x}_s(t) = \bar{C}_1 x(t) + \bar{D}_{11} w(t) + \bar{D}_{12} u(t)$$
(8)

where

$$\bar{C}_1 = \left[ \begin{array}{cccc} -k_s/m_s & -c_s/m_s & 0 & c_s/m_s & 0 & 0 \end{array} \right],$$
 
$$\bar{D}_{11} = 0, \quad \bar{D}_{12} = 1/m_s$$

#### (ii) Constraint outputs:

$$y_2(t) = \bar{C}_2 x(t) + \bar{D}_{21} w(t) + \bar{D}_{22} u(t)$$
 (9)

$$\bar{C}_2 = \left[ \begin{array}{cccc} \frac{1}{S_{\max}} & 0 & 0 & 0 & 0 & 0 \\ 0 & 0 & \frac{k_t}{(m_s + m_u + m_d)g} & 0 & 0 & 0 \\ 0 & 0 & 0 & 0 & 0 & 0 \end{array} \right],$$

$$\bar{D}_{21} = \begin{bmatrix} 0 \\ 0 \\ 0 \end{bmatrix}, \quad \bar{D}_{22} = \begin{bmatrix} 0 \\ 0 \\ 1/u_{\max} \end{bmatrix}$$

Output feedback is adopted, with the measurement outputs selected as follows:

$$y_3(t) = \begin{bmatrix} \dot{x}_s(t) & \dot{x}_u(t) \end{bmatrix}^T$$
$$= \bar{C}_3 x(t)$$
(10)

where

$$\bar{C}_3 = \left[ \begin{array}{ccccc} 0 & 1 & 0 & 0 & 0 & 0 \\ 0 & 0 & 0 & -1 & 0 & 0 \end{array} \right]$$

**Remark 2:** The analysis of piecewise affine systems based on a common quadratic Lyapunov function is often overly conservative. Reference (Hassibi and and Boyd, 1998) highlights that for piecewise affine systems, incorporating the ellipsoidal domain information into the stability conditions during controller design can reduce conservatism and effectively address the affine terms. This approach can be reformulated as an LMI representation that is computationally tractable. The reason is that when  $x(t) \in \aleph_j$ ,  $\xi_j$  does not need to hold over the entire state space but only within the specified domain  $\aleph_j$ .

# Design of output feedback $H_{\infty}/GH_2$ Control

To design a controller that ensures asymptotic stability of the system, minimizes the control output, and satisfies time-domain hard constraints. Specifically, minimize the  $H_{\infty}$  norm of the closed-loop transfer function from the road excitation w(t) to the control output  $y_1(t)$ . In addition, the  $GH_2$  norm of the closed-loop transfer function from w(t) to the constraint outputs  $y_2(t)$  should be less than 1. This ensures an optimal trade-off between control performance and the satisfaction of system constraints.

Define  $G_{wy1}(s)$  and  $T_{wy2}(s)$  as the closed-loop transfer function from w(t) to  $y_1(t)$ , and from w(t) to  $y_2(t)$ , respectively. The control objective can be described as follows:

minimize 
$$\|G_{wy1}\|_{\infty}$$
  
 $s.t.$   $\|T_{wy2}\|_{g} < \gamma$  (11)

The constraint output  $y_2(t)$  in Eq.(9) has been normalized, so  $||y_2(t)|| < 1$ , i.e.,  $\gamma = 1$ .

The constraints of most partitions (except for the origin-included partition) are asymmetric, i.e.  $F_j \neq -\overline{F_j}$ , whereas the LMI primarily addresses zero-symmetric constraint problems. According to (Hassibi et al., 1998), the controller can be designed in the following form:

$$u_j(t) = K_j y_3(t) + \xi_j, \quad \xi_j = \frac{\overline{F_j} + \underline{F_j}}{2}$$
 (12)

where  $\xi_j$  is the affine term, from Eq.(12), the following can be obtained:

$$\frac{F_j - \overline{F_j}}{2} \le K_j y_3 \le \frac{\overline{F_j} - F_j}{2} \tag{13}$$

Therefore, the asymmetric constraints on  $u_j(t)$  are converted into symmetric constraints on  $K_iy_3(t)$ .

Substituting Eq.(12) into Eqs.(7)-(9), the following can be obtained:

$$\dot{x}(t) = \tilde{A}x(t) + \bar{B}_1w(t) + \bar{B}_2\xi_j$$
 (14)

$$y_1(t) = \tilde{C}_1 x(t) + \bar{D}_{11} w(t) + \bar{D}_{12} \xi_i \tag{15}$$

$$y_2(t) = \tilde{C}_2 x(t) + \bar{D}_{21} w(t) + \bar{D}_{22} \xi_j$$
 (16)

where

$$\tilde{A} = \bar{A} + \bar{B}_2 * K_j * \bar{C}_3, \quad \tilde{C}_1 = \bar{C}_1 + \bar{D}_{12} * K_j * \bar{C}_3,$$
 
$$\tilde{C}_2 = \bar{C}_2 + \bar{D}_{22} * K_j * \bar{C}_3$$

**Theorem 1:** Assume x(0)=0, the closed-loop system described by Eq.(14) is asymptotically stable, the  $H_{\infty}$  norm of the closed-loop transfer function from w(t) to the control output  $y_1(t)$  is less than  $\rho$ , and the  $GH_2$  norm of the closed-loop transfer function from w(t) to the constraint outputs  $y_2(t)$  is less than 1. This is equivalent to the existence of scalars  $\lambda_j < 0$ , a positive definite symmetric matrix Q, and matrices  $F_j$  of appropriate dimensions, such that the following condition holds:

minimize 
$$\rho^2$$
 (17)

For the origin excluded partitions:

$$\begin{bmatrix} Q_{11} & * & * \\ \left(\lambda_{j}\bar{B}_{2}^{T}\xi_{j}f_{j}^{T} + QE_{j}^{T}\right)^{T} & -\lambda_{j}\left(1 - f_{j}f_{j}^{T}\right) & * \\ \bar{C}_{1}Q + \bar{D}_{12}F_{j}\bar{C}_{3} & 0 & -I \end{bmatrix} < 0$$
(18)

where

$$Q_{11} = QA^{T} + AQ + \bar{C}_{3}^{T} F_{j}^{T} \bar{B}_{2}^{T} + \bar{B}_{2} F_{j} \bar{C}_{3}$$

$$+ \lambda_{j} \bar{B}_{2} \xi_{j} \xi_{j}^{T} \bar{B}_{2}^{T} + \rho^{-2} \bar{B}_{1} \bar{B}_{1}^{T}$$

$$\begin{bmatrix} Q & * \\ \bar{C}_{2} Q + \hat{D}_{22} F_{j} \bar{C}_{3} & \gamma^{2} I \end{bmatrix} > 0$$
(19)

For the origin included partitions

$$\begin{bmatrix} Z_{11} & * & * \\ \bar{B}_{1}^{T} & -\rho^{2} & * \\ \bar{C}_{1}Q + \bar{D}_{12}F_{j}\bar{C}_{3} & 0 & -I \end{bmatrix} < 0$$
 (20)

where

$$Z_{11} = Q\bar{A}^T + \bar{A}Q + \bar{C}_3^T F_i^T \bar{B}_2^T + \bar{B}_2 F_i \bar{C}_3$$

$$\left[\begin{array}{cc}Q&*\\\bar{C}_2Q+\hat{D}_{22}F_j\bar{C}_3&\gamma^2I\end{array}\right]>0$$

If the optimal solution  $(\rho^*, Q^*, F_j^*)$  exists, the static output feedback controller gain is given by:

$$K^* = F_i^* * (V^*)^{-1} (21)$$

where  $V^* = (\bar{C}_3 Q^* \bar{C}_3^T) (\bar{C}_3 \bar{C}_3^T)^{-1}$ 

**Proof:** 

Firstly, the design of the  $H_{\infty}$  control is introduced, along with the proofs for inequalities (18) and (20), which ensure the asymptotic stability of the system and minimize  $\|G_{wy1}\|_{\infty}$ . Subsequently, the  $GH_2$  control is applied, and the proof for inequality (19) is presented, ensuring that the system satisfies  $\|T_{wy2}\|_{o} < 1$ .

## (i) Output feedback $H_{\infty}$ control

Define

$$\|G_{wy1}\|_{\infty} := \sup_{w(t) \in L_2} \frac{\|y_1(t)\|_2}{\|w(t)\|_2} < \rho$$
 (22)

The  $H_{\infty}$  norm is the peak value of the maximum singular value of the system's frequency response. Therefore,

$$\|G_{wy1}\|_{\infty} := \sup_{w(t) \in L_2} \frac{\|y_1(t)\|_2}{\|w(t)\|_2} = \sup_{w(t) \in L_2} \frac{\|\tilde{y}_1(t)\|_2}{\|w(t)\|_2}$$

$$= \sup_{w(t) \in L_2} \left\|\tilde{C}_1 \left(sI - \frac{1}{\tilde{A}^{-1}\bar{B}_1}\right)\right\|_{\infty}$$
(23)

where

$$\tilde{y}_1^T(t)\tilde{y}_1(t) = \left[\tilde{C}_1 x(t)\right]^T \left[\tilde{C}_1 x(t)\right]$$
 (24)

Therefore, system (14) is asymptotically stable, and the  $H_{\infty}$  norm shown in Eq.(23) is less than  $\rho$  if there exists a Lyapunov function  $V(x)=x^TPx$ ,  $P=P^T>0$ , such that

$$\dot{V}(x(t)) + \tilde{y}_1^T(t)\tilde{y}_1(t) - \rho^2 w^T(t)w(t) < 0$$
 (25)

Substituting Eq.(14) yields:

$$\left[ \left( \bar{A} + \bar{B}_2 * K_j * \bar{C}_3 \right) x + \bar{B}_1 w + \bar{B}_2 \xi_j \right]^T P x 
+ x^T P \left[ \left( \bar{A} + \bar{B}_2 * K_j * \bar{C}_3 \right) x + \bar{B}_1 w + \bar{B}_2 \xi_j \right] 
+ \tilde{y}_1^T (t) \tilde{y}_1 (t) - \rho^2 w^T (t) w (t) < 0$$
(26)

Inequality (26) can be rewritten as:

$$\begin{bmatrix} x \\ w \\ 1 \end{bmatrix}^{T} \begin{bmatrix} \tilde{A}^{T}P + P\tilde{A} + \tilde{C}_{1}^{T}\tilde{C}_{1} & * & * \\ \tilde{B}_{1}^{T}P & -\rho^{2}I & * \\ \xi_{j}\bar{B}_{2}^{T}P & 0 & 0 \end{bmatrix} \begin{bmatrix} x \\ w \\ 1 \end{bmatrix} < 0$$
(27)

where \* denotes the symmetric terms in the matrix.

According to **Remark 2**, in order to reduce the conservatism in the controller design,  $\aleph_j$  can be outer approximated by ellipsoids:

$$\varpi_j := \{ x \mid ||E_j x + f_j|| \le 1 \}$$
(28)

where

$$E_{j} = 2\varepsilon / (x_{Rj} - x_{Lj}),$$

$$\varepsilon = \begin{bmatrix} 0 & 1 & 0 & -1 & 0 & 0 \end{bmatrix},$$

$$f_{j} = -(x_{Rj} + x_{Lj}) / (x_{Rj} - x_{Lj})$$

Applying the S-procedure to inequality (27) the following can be obtained:

$$\begin{bmatrix}
\Theta_1 & * & * \\
\bar{B}_1^T P & -\rho^2 I & * \\
\xi_j \bar{B}_2^T P + \lambda_j f_j^T E_j & 0 & \lambda_j \left( f_j^T f_j - 1 \right)
\end{bmatrix} < 0$$
(29)

where  $\lambda_i < 0$ ,

$$\Theta_1 = \tilde{A}^T P + P \tilde{A} + \tilde{C}_1^T \tilde{C}_1 + \lambda_j E_j^T E_j$$

It can be observed that inequality (29) contains nonlinear terms, i,e,, $K_j * P$ , the following section will address the linearization.

Define  $Q = Q^T = P^{-1}$ , premultiplying and postmultiplying (29) by diag $\{Q, I, I\}$ , the following can be obtained:

$$\begin{bmatrix} \Theta_2 & * & * \\ \bar{B}_1^T & -\rho^2 I & * \\ \xi_j \bar{B}_2^T + \lambda_j f_j^T E_j Q & 0 & \lambda_j \left( f_j^T f_j - 1 \right) \end{bmatrix} < 0$$

$$(30)$$

where

$$\Theta_2 = Q\tilde{A}^T + \tilde{A}Q + Q\tilde{C}_1^T\tilde{C}_1Q + \lambda_i QE_i^TE_iQ$$

Applying the Schur complement twice, inequality (30) can be transformed into:

$$\Phi_{j} + \lambda_{j}^{-1} \left( \bar{B}_{2} \xi_{j} + \lambda_{j} Q E_{j}^{T} f_{j} \right) \left( 1 - f_{j}^{T} f_{j} \right)^{-1}$$

$$\left( \bar{B}_{2} \xi_{j} + \lambda_{j} Q E_{j}^{T} f_{j} \right)^{T} + \rho^{-2} \bar{B}_{1} \bar{B}_{1}^{T} + \lambda_{j} Q E_{j}^{T} E_{j} Q < 0$$
(31)

According to the matrix inverse lemma, i.e.,

$$(I - f_i^T f_i)^{-1} = I + f_i^T (I - f_i f_i^T)^{-1} f_i$$

$$f_i^T (I - f_i f_i^T)^{-1} = (I - f_i^T f_i)^{-1} f_i^T$$
(32)

Inequality (31) can be reorganized as:

$$\Phi_{j} + \lambda_{j}^{-1} \left( \lambda_{j} \bar{B}_{2} \xi_{j} f_{j}^{T} + Q E_{j}^{T} \right) \left( 1 - f_{j} f_{j}^{T} \right)^{-1}$$

$$\left( \lambda_{j} \bar{B}_{2} \xi_{j} f_{j} + Q E_{j}^{T} \right)^{T} + \rho^{-2} \bar{B}_{1} \bar{B}_{1}^{T}$$

$$+ \lambda_{j} \bar{B}_{2} \xi_{j} \left( \bar{B}_{2} \xi_{j} \right)^{T} < 0$$
(33)

Applying the Schur complement to inequality (33), yields:

$$\begin{bmatrix} \Theta_{3} & * & * \\ \left(\lambda_{j}\bar{B}_{2}^{T}\xi_{j}f_{j}^{T} + QE_{j}^{T}\right)^{T} & -\lambda_{j}\left(1 - f_{j}f_{j}^{T}\right) & * \\ \bar{C}_{1}Q + \left(\bar{D}_{12}K_{j}\bar{C}_{3}\right)Q & 0 & -I \end{bmatrix} < 0$$
(34)

where

$$\Theta_3 = Q\tilde{A}^T + \tilde{A}Q + \lambda_j \bar{B}_2 \xi_j \xi_j^T \bar{B}_2^T + \rho^{-2} \bar{B}_1 \bar{B}_1^T$$

Inequality (34) still contains nonlinear terms, i.e.,  $K_j * Q$ . Applying  $V\bar{C}_3 = \bar{C}_3Q$ ,  $F_j = K_jV$ , inequality (34) is equivalent to (18).

Therefore, for the origin-excluded partitions, the sufficient condition for system stability and the  $H_{\infty}$  norm is that there exist  $Q = Q^T > 0$ ,  $\rho > 0$ , and  $\lambda_j < 0$  such that the LMI in (18) holds.

For the origin-included partition, the damping force constraint is symmetric, and the affine term is zero. The sufficient condition for the origin-included partition can be deduced as: if there exist  $Q=Q^T>0,\, \rho>0$ , such that the LMI in (20) holds.

If inequalities (18) and (20) hold, then (25) can be obtained, i.e.,

$$\dot{V}(x(t)) + \tilde{y}_1^T(t)\tilde{y}_1(t) - \rho^2 w^T(t)w(t) < 0$$

Integrating both sides of (25) from 0 to t gives:

$$\int_{0}^{t} \|\tilde{y}_{1}(\tau)\|^{2} d\tau - \rho^{2} \int_{0}^{t} \|w(\tau)\|^{2} d\tau + V(x(t)) - V(x(0)) < 0$$
(35)

Applying  $w \in L_2[0,\infty]$ , if  $t \to \infty$  in (35) and with initial state x(0)=0, it follows that V(x(0))=0, Additionally, since  $V(x(\infty))>0$ , we have:

$$\int_{0}^{\infty} \|\tilde{y}_{1}(\tau)\|^{2} d\tau - \rho^{2} \int_{0}^{\infty} \|w(\tau)\|^{2} d\tau < 0$$
 (36)

According to Eq.(23), it follows that  $\|G_{wy1}\|_{\infty} < \rho$ .

**Remark 3:** The stability of switching between controllers can be guaranteed by defining a global quadratic Lyapunov function.

**Remark 4:** In the case of origin-included partitions, where  $\lambda_j < 0$ , Eq.(29) is infeasible. Moreover, in origin-included partitions, the damping force approximation is symmetric about the origin, resulting in the affine term being zero. Therefore, categorizing controller design into "origin-included partitions" and "origin-excluded partitions" is essential to ensure both mathematical feasibility and modeling accuracy.

# (ii) The maximum magnitude of the constraint output and the $GH_2$ norm of the system

From Eq.(16), the constraint output is:

$$y_{2} = \begin{bmatrix} \frac{x_{s} - x_{u}}{S_{\text{max}}} & \frac{k_{u}(x_{u} - x_{r})}{(m_{s} + m_{u} + m_{d})g} & \frac{u_{j}}{u_{j \text{ max}}} \end{bmatrix}^{T}$$

$$= \bar{C}_{2}x(t) + \bar{D}_{22}u_{j}(t)$$
(37)

where

$$\bar{C}_2 = \left[ \begin{array}{cccc} \frac{1}{S_{\max}} & 0 & 0 & 0 & 0 & 0 \\ 0 & 0 & \frac{k_t}{(m_s + m_u + m_d)g} & 0 & 0 & 0 \\ 0 & 0 & 0 & 0 & 0 & 0 \end{array} \right],$$

$$\bar{D}_{22} = \begin{bmatrix} 0 \\ 0 \\ 1/u_{j\max} \end{bmatrix}$$

Define

$$\hat{u}_i = K_i y_3 \tag{38}$$

then

$$\frac{q_{Lj} - q_{Uj}}{2} \le \hat{u}_j \le \frac{q_{Uj} - q_{Lj}}{2}$$

The constraint output in (37) can be transformed into:

$$\tilde{y}_2 = \begin{bmatrix} \frac{x_s - x_u}{S_{\text{max}}} & \frac{k_u(x_u - x_r)}{(m_s + m_u)g} & \frac{\hat{u}_j}{\hat{u}_{j \text{ max}}} \end{bmatrix}^T$$

$$= \bar{C}_2 x(t) + \hat{D}_{22} \hat{u}_i(t)$$
(39)

where

$$\hat{D}_{22} = \begin{bmatrix} 0 \\ 0 \\ 1/\hat{u}_{i \max} \end{bmatrix}$$

From (11), the  $GH_2$  norm from w(t) to  $\tilde{y}_2(t)$  is:

$$\|T_{w\tilde{y}_2}\|_g := \sup_{w \in L_2} \frac{\|\tilde{y}_2\|_{\infty}}{\|w\|_2} < \gamma \tag{40}$$

where  $\|\tilde{y}_2\|_{\infty}$  is defined as:

$$\|\tilde{y}_2\|_{\infty} := \max_{i=1,2,\dots,n} \sup_{t>0} |\tilde{y}_{2i}|$$
 (41)

For system (14), with  $\gamma = 1$  and the initial state x(0) = 0, the following two conditions are equivalent:

1): The system is asymptotically stable; The  $GH_2$  norm of the closed-loop transfer function from w(t) to constraint output  $\tilde{y}_2(t)$ , i.e.,  $||T_{w\tilde{u}_2}||_2 < 1$ ;

output  $\tilde{y}_2(t)$ ,i.e.,  $\|T_{w\tilde{y}_2}\|_g < 1$ ;

2): If and only if there exists a positive definite matrix  $P = P^T$ , such that the following condition holds:

$$\begin{bmatrix} \tilde{A}^T P + P\tilde{A} & * & * \\ \bar{B}_1^T P & -I & * \\ \xi_j \bar{B}_2^T P & 0 & 0 \end{bmatrix} < 0$$
 (42)

$$\begin{bmatrix} P & * \\ \bar{C}_2 + \hat{D}_{22}K_j\bar{C}_3 & \gamma^2 I \end{bmatrix} > 0 \tag{43}$$

Condition 1) is verified through condition 2) by the following process:

Define  $V(x) = x^T P x$ ,  $P = P^T > 0$ 

Premultiplying (42) by  $\begin{bmatrix} x^T(t) & w^T(t) & 1 \end{bmatrix}$  and post-multiplying by  $\begin{bmatrix} x^T(t) & w^T(t) & 1 \end{bmatrix}^T$ , the following can be obtained:

$$\left[ \left( \bar{A} + \bar{B}_2 * K_j * \bar{C}_3 \right) x + \bar{B}_1 w + \bar{B}_2 \xi_j \right]^T P x 
+ x^T P \left[ \left( \bar{A} + \bar{B}_2 * K_j * \bar{C}_3 \right) x + \bar{B}_1 w + \bar{B}_2 \xi_j \right] 
- w^T w < 0$$
(44)

i.e.,

$$\dot{V}(t) - w^T(t)w(t) < 0 \tag{45}$$

Integrating both sides of (45) from 0 to t gives:

$$x^{T}(t)Px(t) < \int_{0}^{t} \|w(\tau)\|^{2} d\tau + x^{T}(0)Px(0)$$
 (46)

With x(0) = 0, (46) is equivalent to:

$$x^{T}(t)Px(t) < \int_{0}^{t} \|w(\tau)\|^{2} d\tau$$
 (47)

Applying Schur, (43) is equivalent to:

$$\left(\bar{C}_2 + \hat{D}_{22}K_j\bar{C}_3\right)^T \left(\bar{C}_2 + \hat{D}_{22}K_j\bar{C}_3\right) < \gamma^2 P$$
 (48)

From (46) to (48), we obtain:

$$\tilde{y}_{2}^{T}(t)\tilde{y}_{2}(t) 
= x^{T}(t) \left(\bar{C}_{2} + \hat{D}_{22}K_{j}\bar{C}_{3}\right)^{T} \left(\bar{C}_{2} + \hat{D}_{22}K_{j}\bar{C}_{3}\right) x(t) 
< \gamma^{2}x^{T}(t)Px(t) 
< \gamma^{2} \int_{0}^{t} \|w(\tau)\|^{2}d\tau 
< \gamma^{2} \int_{0}^{\infty} \|w(\tau)\|^{2}d\tau$$
(49)

Inequality (49) holds for all  $t \in [0, \infty)$ . According to (40),  $\|T_{w\tilde{y}_2}\|_q < \gamma$ .

Premultiplying and postmultiplying (43) by diag  $\{P^{-1}, I\}$ , (19) is obtained, i.e.,

$$\left[\begin{array}{cc}Q & *\\ \bar{C}_2Q + \hat{D}_{22}F_j\bar{C}_3 & \gamma^2I\end{array}\right] > 0$$

**Remark 5:** For origin-excluded partitions, if inequality (18) holds, (42) follows. For origin-included partitions, if inequality (20) holds, (42) follows. Therefore, it is sufficient to satisfy inequality (43).

#### Simulation results

In this section, the proposed output feedback  $H_{\infty}/GH_2$  controller is applied to the aforementioned quarter-vehicle IWM driven semi-active suspension system. Based on the GBT 4970-2009 "Automobile Ride Comfort Test Methods" and the European ISO 2632 standard, simulations are conducted, including bump pulse input, road with waves, and random road excitation.

The total partition number N is set to 9, 15, 21, respectively. Table 3 compares the root mean square (RMS) values of the vehicle body vertical acceleration for different N. The comparative experiments are conducted with skyhook control and a passive suspension system.

Figs.4-9 present the simulation results for bump, road wave, and C-grade road excitation when N=15.

# Simulation analysis of bump road excitation

The simulation of bump road is used to characterize the suspension control performance under the discrete impact road excitation. The mathematical description is as follows:

$$x_r(t) = \begin{cases} \frac{A}{2} \left( 1 - \cos \frac{2\pi V(t - t_0)}{L} \right) & t_0 \le t \le \frac{L}{V} + t_0 \\ 0 & \text{otherwise} \end{cases}$$
(50)

with a height of A = 0.04m, and a width of L = 0.3m, where  $t_0$  is the time when the vehicle enters the bump.

When the vehicle passes the bump at V=8.3m/s, the time-domain responses of the in-wheel motor semi-active suspension are shown in Fig.4 and Fig.5.

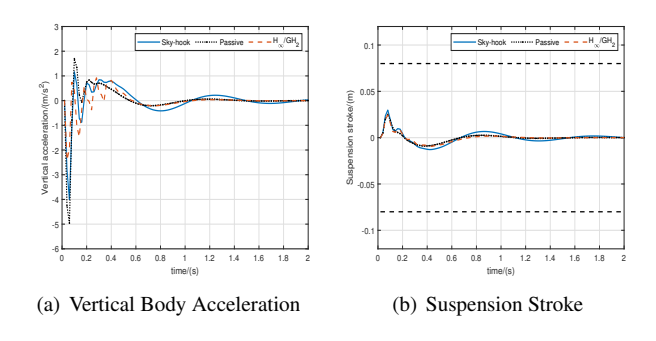
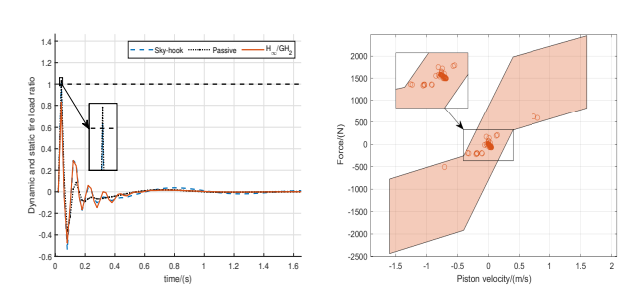


Figure 4. Vibration performance with bump road excitation



(a) Dynamic-to-static tire load ratio (b) Piston Velocity-Damping Force

Figure 5. Vibration performance with bump road excitation

All the  $H_{\infty}/GH_2$  control, sky-hook control, and the passive suspension satisfy the suspension stroke constraints.

However, as shown in Fig.5(a), the dynamic-to-static tire load ratio of both the sky-hook control and passive suspension violates the constraints, resulting in the wheels to lift off the ground, which severely impacts the vehicle's handling stability. In contrast, the  $H_{\infty}/GH_2$  control remains within the constraint limits.

**Table 3.** P2P Values of Vertical Body Acceleration On Bump Road Excitation.

Road Excitation	Sky-hook	Passive	$H_{\infty}/GH_2$
Bump	4.9204	7.6558	3.3337

To evaluate the ride comfort of different suspension systems under bump road excitation, the peak-to-peak (P2P) values of vertical body acceleration are presented in Tables 3. It quantifies the total fluctuation in vertical body acceleration, providing the overall dynamic response of the vehicle. The P2P value is defined as (Feng et al., 2023):

$$P2P = a_{max} - a_{min}$$

where  $a_{max}$  and  $a_{min}$  represent the maximum and minimum values of the vertical body acceleration, respectively.

Table 3 shows that the proposed control further decreases the P2P value to 3.3337, a 32.3% reduction relative to the sky-hook control and over 56% compared to the passive suspension, which demonstrates the robustness of the  $H_{\infty}/GH_2$  control.

Table 4 compares the RMS values of the vertical acceleration of the vehicle body under different N. For bump road and road wave excitation, the semi-active suspension with  $H_{\infty}/GH_2$  control with N=15 significantly reduces the vertical acceleration compared to both the passive suspension and the semi-active suspension with sky-hook control. Furthermore, Fig.5(b) illustrates that the output damping force satisfies the dissipative constraint of the MR damper.

In addition, the ride comfort at N=9 and N=21 is noticeably inferior to that at N=15, highlighting the critical role of selecting an appropriate partition number N in piecewise linear systems.

The simulation results demonstrate that the proposed output feedback  $H_{\infty}/GH_2$  control strategy significantly improves the performance of the in-wheel motor driven semi-active suspension system, while also validating the effectiveness of the piecewise linearization method.

# Simulation analysis of road waves excitation

The mathematical description is given by Eq.(50), with a height of A = 0.11m, and a width of L = 5m. The simulation results are shown in Fig.6 and Fig.7.

When the vehicle passes over road waves at V=16.7m/s, Fig.6(a) indicates that the passive suspension provides the worst ride comfort. As shown in Table 4, the semi-active suspension with the  $H_{\infty}/GH_2$  control with N=15 provides the best comfort. Fig.6(b) shows that both the semi-active suspension with sky-hook control and the passive suspension violate the suspension stroke constraint, while the semi-active suspension with the  $H_{\infty}/GH_2$  control remains within the constraint limits. Fig.7(a) illustrates that the passive suspension approaches the upper constraint limit

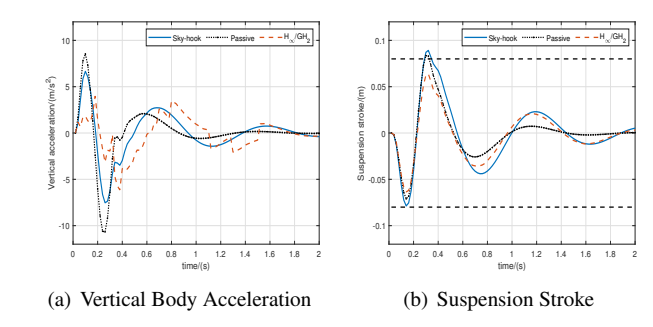
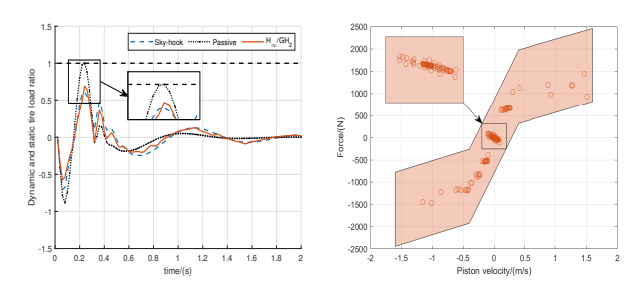


Figure 6. Vibration performance with road waves excitation



(a) Dynamic-to-static tire load ratio (b) Piston Velocity-Damping Force

Figure 7. Vibration performance with road waves excitation

at 0.3s, with the tire about to lift off the ground. In contrast, the semi-active suspension with sky-hook control has better performance, and the semi-active suspension with  $H_{\infty}/GH_2$  control stays well within the constraint limits. Fig.7(b) demonstrates that the output damping force satisfies the dissipative constraint of the MR damper, further validating the effectiveness of the piecewise linearization method.

# Simulation analysis of C-grade road excitation

When the vehicle passes C-grade road excitation at V=18m/s, Fig.8(b) shows that the passive suspension is more effective in suppressing the suspension stroke. Although the semi-active suspension with sky-hook control and  $H_{\infty}/GH_2$  control perform slightly worse than the passive suspension, they still remain within the mechanical structure constraints.

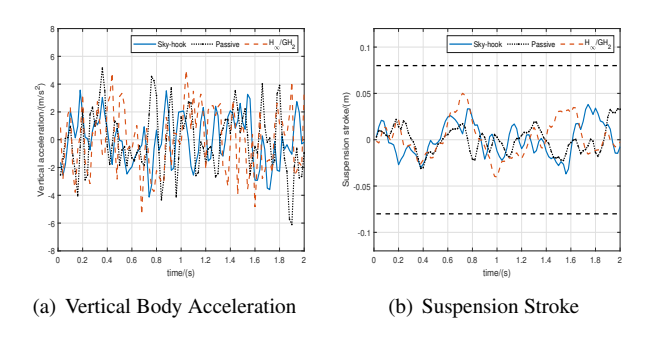
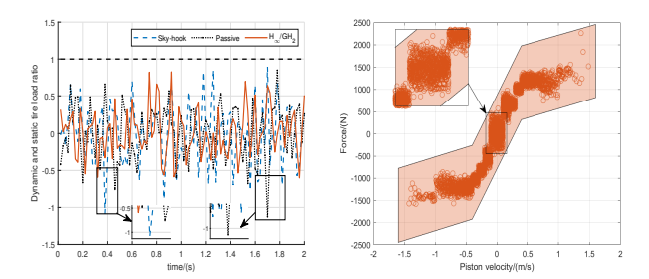


Figure 8. Vibration performance with C-grade road excitation

From Fig.8(a) and Table 4, for the C-grade road excitation, the sky-hook control provides the best comfort. Fig.9(a) reveals that the dynamic-to-static tire load ratio of both

Table 4. RMS Values of Vertical Body Acceleration Under Different Excitation.

Road Excitation	Sky-hook	Passive	$H_{\infty}/GH_2(N=9)$	$H_{\infty}/GH_2(N=15)$	$H_{\infty}/GH_2(N=21)$
Bump	0.0861	0.1243	0.0910	0.0612	0.1054
Road waves	0.3424	0.3932	0.2753	0.2694	0.2754
C-grade	1.9402	2.8667	2.2673	2.2624	2.1968



(a) Dynamic-to-static tire load ratio (b) Piston Velocity-Damping Force

Figure 9. Vibration performance with C-grade road excitation

the semi-active suspension with sky-hook control and the passive suspension violates the constraint limits. In contrast, the semi-active suspension with  $H_{\infty}/GH_2$  control remains within the constraints. Fig.9(b) shows that the dissipative constraint of the MR damper are satisfied.

Therefore, a balance between ride comfort and handling stability is achieved through the proposed  $H_{\infty}/GH_2$  control.

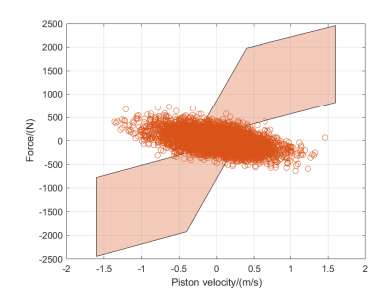


Figure 10. Piston Velocity/damping force characteristic of the MR damper with conventional  $H_{\infty}$  control

To demonstrate the contribution of this paper, Fig.10 shows the piston velocity–damping force relationship of the MR damper with conventional  $H_{\infty}$  control, subjected to C-grade road excitation. It clearly violates the dissipative property of the MR damper and reduces system performance, which confirms the necessity of addressing the dissipative constraints. This issue would be even more pronounced in testbed experiments. However, due to equipment limitations, testbed experiments could not be conducted in this study. Future work will focus on validating the proposed control strategy through testbed experimentation.

# **Conclusions**

In IWM driven electric vehicles, the increased unsprung mass often leads to negative vibration in ride comfort and handling stability. To address this challenge, an output feedback  $H_{\infty}/GH_2$  control strategy was proposed. The

nonlinear constraints of the MR damper were approximated using piecewise constant constraints. Simulation results demonstrate that the proposed piecewise linearization method effectively addresses the dissipative constraint of the semi-active suspension system. Compared to the semi-active suspension with sky-hook control and the passive suspension, the semi-active suspension with  $H_{\infty}/GH_2$  control not only satisfies the mechanical structure limitations and handling stability requirements but also significantly improves ride comfort. On the other hand, this work was overlooked the coupling of electromagnetic forces in inwheel motors, which will be a focus of future research.

#### Acknowledgements

This work was supported by the National Natural Science Foundation of China (No.62473167), and the Science Foundation of Jilin Province (No.20240402079GH).

#### **Declaration of conflicting interests**

The author(s) declared no potential conflicts of interest with respect to the research, authorship, and/or publication of this article.

#### References

Mishra S, Varshney A, Singh B, et al. (2022) Driving-Cycle-Based Modeling and Control of Solar-Battery-Fed Reluctance Synchronous Motor Drive for Light Electric Vehicle With Energy Regeneration. *IEEE Transactions on Industry Applications* 58:6666-6675.

Cai S, Kirtley JL and Lee CH (2022) Critical Review of Direct-Drive Electrical Machine Systems for Electric and Hybrid Electric Vehicles. *IEEE Transactions on Energy Conversion* 37(4):2657-2668.

Xiao ZX, Hu MH, Chen S, et al. (2024) Bearing Electrical-Erosion Damage in Electrical Drive Systems: A Review. *IEEE Transactions on Transportation Electrification* 10(2):3428-3442.

Huynh TA, Chen PH and Hsieh MF (2022) Analysis and Comparison of Operational Characteristics of Electric Vehicle Traction Units Combining Two Different Types of Motors. IEEE Transactions on Vehicular Technology 71(6):5727-5742.

Mahmouditabar F, Vahedi A and Takorabet N (2022) Design and Analysis of Interior Permanent Magnet Motor for Electric Vehicle Application Considering Irreversible Demagnetization. *IEEE Transactions on Industry Applications* 58(1):284-293.

Nagaya G, Wakao Y and Abe A (2003) Development of an inwheel drive with advanced dynamic-damper mechanism. *JSAE Review* 24(4):477-481.

Li Z, Zheng L, Ren Y, et al. (2019) Multi-objective optimization of active suspension system in electric vehicle with In-Wheel-Motor against the negative electromechanical coupling effects. *Mechanical Systems and Signal Processing* 116:545-565.

Qin YC, He CC, Ding P, et al. (2018) Suspension hybrid control for in-wheel motor driven electric vehicle with dynamic vibration absorbing structures. *IFAC-PapersOnLine* 51:973-978.

- Shao XX, Naghdy F and Du HP (2017) Reliable fuzzy  $H_{\infty}$  control for active suspension of in-wheel motor driven electric vehicles with dynamic damping. *Mechanical Systems and Signal Processing* 87:365-383.
- Jin XJ, Wang JD, He XK, et al. (2023) Improving Vibration Performance of Electric Vehicles Based on In-Wheel Motor-Active Suspension System via Robust Finite Frequency Control. *IEEE Transactions on Intelligent Transportation* Systems 24(2):1631-1643.
- Vidal V, Stano P, Tavolo G, et al. (2022) On Pre-Emptive In-Wheel Motor Control for Reducing the Longitudinal Acceleration Oscillations Caused by Road Irregularities. *IEEE Transactions* on Vehicular Technology 71(9):9322-9337.
- Zhang B and Su XP (2024) Dynamic modeling and elastic characteristic analysis of the transverse leaf spring suspension. *Journal of Mechanical Science and Technology* 38:1051–1058.
- Min DL and Wei YT (2024) An adaptive control strategy for a semiactive suspension integrated with intelligent tires. *Mechanical Systems and Signal Processing* 212:111281.
- Yuan Q, Zhou HL, Chen SL, et al. (2023) Designing a Switched Takagi-Sugeno Fuzzy controller for CDC semi-active suspensions with current input constraint. *Mechanical Systems* and Signal Processing 199:110450.
- Jin TH, Liu ZM, Sun SS, et al. (2020) Development and evaluation of a versatile semi-active suspension system for high-speed railway vehicles. *Mechanical Systems and Signal Processing* 135:06338.
- Ma KW, Xu FY, Zhou YR, et al. (2024) Design, dynamic modeling and testing of a novel MR damper for cable-stayed climbing robots under wind loads. *ISA Transactions*.
- Yang HH, Liu QW, Zhang YC, et al. (2023) An adaptive sliding mode fault-tolerant control for semi-active suspensions with magnetorheological dampers based on T-S fuzzy vehicle models. *Journal of Vibration and Control* 29(1-2):251-264.
- Savaia G, Sohn Y, Formentin S, et al. (2021) Experimental automatic calibration of a semi-active suspension controller via Bayesian Optimization. *Control Engineering Practice* 112:104826.
- Ma XB, Wong PK and Zhao J (2019) Practical multi-objective control for automotive semi-active suspension system with nonlinear hydraulic adjustable damper. *Mechanical Systems* and Signal Processing 117:667-688.
- Yoon DS, Kim GW and Choi SB (2021) Response time of magnetorheological dampers to current inputs in a semi-active suspension system: Modeling, control and sensitivity analysis. *Mechanical Systems and Signal Processing* 146.
- Ding RK, Wang RC, Meng XP, et al. (2023) Research on time-delay-dependent  $H_{\infty}/H_2$  optimal control of magnetorheological semi-active suspension with response delay. *Journal of Vibration and Control* 29(5-6):1447-1458.
- Wu J, Zhou HL, Liu ZY, et al. (2020) Ride Comfort Optimization via Speed Planning and Preview Semi-Active Suspension Control for Autonomous Vehicles on Uneven Roads. *IEEE Transactions on Vehicular Technology* 69(8): 8343-8355.
- Wu J, Zhou HL, Liu ZY, et al. (2019) A load-dependent PWA- $H_{\infty}$  controller for semi-active suspensions to exploit the performance of MR dampers. *Mechanical Systems and Signal*

Processing 127:441-462.

- Nguyen SD, Lam BD and Ngo VH (2020) Fractional-order sliding-mode controller for semi-active vehicle MRD suspensions. *Nonlinear Dynamics* 101:795–821.
- Nguyen SD, Lam BD and Choi SB (2021) Smart dampers-based vibration control–Part 2: Fractional-order sliding control for vehicle suspension system. *Mechanical Systems and Signal Processing* 148:107145.
- Lee D, Jin S and Lee C (2023) Deep Reinforcement Learning of Semi-Active Suspension Controller for Vehicle Ride Comfort. *IEEE Transactions on Vehicular Technology* 72(1):327-339.
- Hassibi A and Boyd S (1998) Quadratic stabilization and control of piecewise-linear systems. *Proceedings of the 1998 American Control Conference. ACC* 3659-3664.
- Feng JJ, Liu BX, Luo XQ, et al. (2023) Experimental investigation on characteristics of cavitation-induced vibration on the runner of a bulb turbine. *Mechanical Systems and Signal Processing* 189:110097.